Quantitative composition and mesoscale ion distribution in p-type organic mixed ionic-electronic conductors

Ruiheng Wu,[1,†] Bryan D. Paulsen,[2,†] Qing Ma,[4] Jonathan Rivnay[2,3*]

[1]Department of Chemistry, Northwestern University, Evanston, IL 60208, USA

[2]Department of Biomedical Engineering, Northwestern University, Evanston, IL 60208, USA

[3]Simpson Querrey Institute, Northwestern University, Chicago, Illinois 60611, USA.

[4]DND-CAT, Synchrotron Research Center, Northwestern University, Evanston, IL, 60208, USA

E-mail: jrivnay@northwestern.edu

[†] The authors contributed equally to this manuscript

Abstract

Understanding the ionic composition and distribution in organic mixed ionic-electronic conductors (OMIECs) is crucial for understanding their structure-property relationships. However, direct measurement of OMIEC ionic composition and distribution is not common. In this work, we investigate the ionic composition and mesoscopic structure of three typical p-type OMIEC materials: an ethylene glycol treated crosslinked OMIEC with large excess fixed anionic charge (EG/GOPS-PEDOT:PSS), an acid treated OMIEC with tunable fixed anionic charge (crys-PEDOT:PSS), and a single component OMIEC absent any fixed anionic charge (pg2T-TT). A combination of X-ray fluorescence (XRF) and photoelectron spectroscopies (XPS), gravimetry, coulometry, and grazing incidence small angle X-ray scattering (GISAXS) techniques were employed to characterize these OMIECs following electrolyte exposure and electrochemical cycling. In particular, XRF provided quantitative ion-to-monomer compositions for these OMIECs from passive ion uptake following aqueous electrolyte exposure, and potential driven ion uptake/expulsion following electrochemical doping and dedoping. Single ion (cation) transport in EG/GOPS-PEDOT:PSS due to Donnan exclusion was directly confirmed, while despite significant fixed anion concentration in crys-PEDOT:PSS doping and dedoping was shown to occur through mixed anion and cation transport. Controlling the fixed anionic (PSS^-) charge density in crys-PEDOT:PSS mapped the strength of Donnan exclusion in OMIEC systems

following a Donnan-Gibbs model. Anion transport dominated pg2T-TT doping and dedoping, but a surprising degree of anionic charge trapping (~10^{20} cm^{-3}) was observed. GISAXS revealed minimal ion segregation both between PEDOT- and PSS-rich domains in EG/GOPS-PEDOT:PSS, and between amorphous and semicrystalline domains in pg2T-TT, but showed significant ion segregation in crys-PEDOT:PSS at length scales of tens of nm, ascribed to inter-nanofibril void space. These results bring new clarity to the ionic composition and distribution of OMIECs that are crucial for accurately connecting structure and properties in these materials.

Introduction

Organic mixed ionic-electronic conductors (OMIECs) are π-conjugated soft materials with ionic or ionophilic functionalization that imparts free ion miscibility and transport. OMIEC's ability to both transport and couple ionic and electronic charge make them attractive active materials for next generation bioelectronics,[1-4] energy storage,[5] electrochromic,[6, 7] and neuromorphic computing applications.[8, 9] There has been a recent growth in characterization work with the aim of unraveling OMIEC structure-property relationships in order to direct synthetic design of OMIECs and improve performance in targeted applications. These efforts are challenging as OMIECs in application relevant conditions are often swollen with ions and solvent, and the resulting electrolyte-swollen structure is sensitive to electrochemical potential and the composition of the surrounding media. While significant advances have improved the understanding of application-relevant structure and electronic transport, significantly less work has explored ionic/solvent composition and transport in OMIECs. This critically limits the development of OMIECs, since understanding the structure property relationships that dictate mixed transport require knowledge of OMIEC composition, especially the concentration and distribution of ionic species.

Previous studies of OMIECs have employed electrochemical quartz crystal microbalance (EQCM) to capture mass/thickness changes.[10-14] Microbalance techniques cannot differentiate between species that contribute to thin film mass changes, thus some studies reporting dopant and solvent concentrations depend on the assumption that counter ion contributions are excluded,[10, 11] though others have found evidence indicating counter ion contributions.[15, 16]

Recent work has employed X-ray photoelectron spectroscopy (XPS) and glow discharge optical emission spectroscopy (GDOES) to quantify the composition of OMIECs.[9, 16, 17] These studies have monitored the passive (not driven by applied potential) uptake of anion-cation pairs,[17] the competition of cation expulsion and anion injection in the electrochemical p-doping processes,[16] and the ion trapping that enables non-volatile electrochemical state retention.[9] These reports give important insights into the fundamental processes in OMIECs. However, they are hindered by high detection limits and difficulties with calibration that constrain them to reporting qualitative results. Thus, quantitative composition determination in OMIECs remains to be achieved. Additionally, the depth profiling involved in both techniques to probe the composition within the OMIEC samples makes them necessarily destructive techniques. This limits the potential adoption of in situ/operando implementations of these techniques to capture the dynamic application relevant composition. Finally, due to the diversity and complexity of OMIEC meso-scale structure,[18] composition throughout OMIEC is not expected to be constant (possible ion segregation between amorphous and crystalline domains, and between polyelectrolyte and conjugated polymer domains). Where ions and solvent molecule segregate is as important as how many ions there are. Thus, bulk OMIEC composition determination should be paired with investigations of component distribution.

In light of these issues, there is a critical need for quantitative non-destructive in situ/operando compatible techniques to measure OMIEC ionic composition and distribution. To this end, synchrotron radiation techniques (especially spectroscopy and scattering) present an attractive means of accomplishing both. X-ray fluorescence (XRF) spectroscopy has been performed in a wide range of elemental analyses, known for being fast, non-destructive, accurate, and is ideal for the quantitative analysis of low concentration elements in thin film samples.[19, 20] Common benchtop XRF instruments often use a fixed incident wavelength, which results in weak fluorescence intensity when the incident photon energy is far from the absorption edge of the target element. In synchrotron light sources, the accuracy of the analysis of the target element at the absorption edge of the element is further improved because of the high brilliance and tunable wavelength of the incident X-rays.[21] Selection of known composition calibrant samples with similar geometry and elemental ratio to the sample of interest[22, 23] enables quantitative elemental analysis of OMIEC samples, and has allowed high precision determination of trace impurities in conjugate polymer based solar cells.[24]

Small angle X-ray scattering with synchrotron sources enables the probing of mesoscale structure. Significant work has been carried out to understand OMIEC as-cast structure, revealing the effect of additives and processing conditions on meso-scale structure,[25, 26] and meso-scale structure formation during film deposition.[27, 28] While in situ work has been reported on the electrochemical potential meso-scale structure in Li^+ transporting block copolymers for battery applications,[29, 30] there have been a noted absence of work reporting small angle scattering in other types of OMIECs exposed to application-relevant conditions in situ or ex situ.

Here we report ex situ XRF and grazing incidence X-ray scattering studies of two prototypical p-type OMIECs: poly(3,4-ethylenedioxythiophene) polystyrene sulfonate (PEDOT:PSS), a dual component OMIEC consisting of a conjugated polymer templated on a polyelectrolyte; and pg2T-TT a single component conjugated polymer electrolyte OMIEC. For both we explore the OMIEC ion composition when the thin films are exposed to electrolytes, and at various electrochemical potentials (dedoped, naturally doped, redoped to a higher oxidation level) relating to degree of oxidation across systematically varied electrolyte concentration and pH. The quantitative determination of the potential/concentration/pH dependent OMIEC composition reveals the role of buffering and Donnan exclusion in polyelectrolyte based OMIECs containing an excess of fixed ionic charge. Additionally, massive amounts of ionic charge trapping compensated by trapped localized electronic charge is revealed in conjugated polymer electrolytes lacking fixed ionic charge. These synchrotron-based ex situ XRF measurements were complimented with benchtop XRF, XPS, and EQCM studies. Further, investigating the composition of record high conductivity acid crystallized PEDOT:PSS (crys-PEDOT:PSS) reveals the limits of Donnan exclusion and the complex composition that accompanies peak OMIEC conductivity.

To investigate the ion distribution ex situ, grazing incidence small angle X-ray scattering (GISAXS) was carried out for both the prototypical systems and record performing crys-PEDOT:PSS. The contrast of GISAXS patterns provides the homogeneity information of the organic film at mesoscale and gives insight into the distribution of ions at different doping levels. These results represent the first quantitative compositional determination of OMIEC ion distribution during electrochemical cycling and establishes quantitative techniques necessary to

produce meaningful structure-property relationships to drive the rational design of next-generation OMIECs.

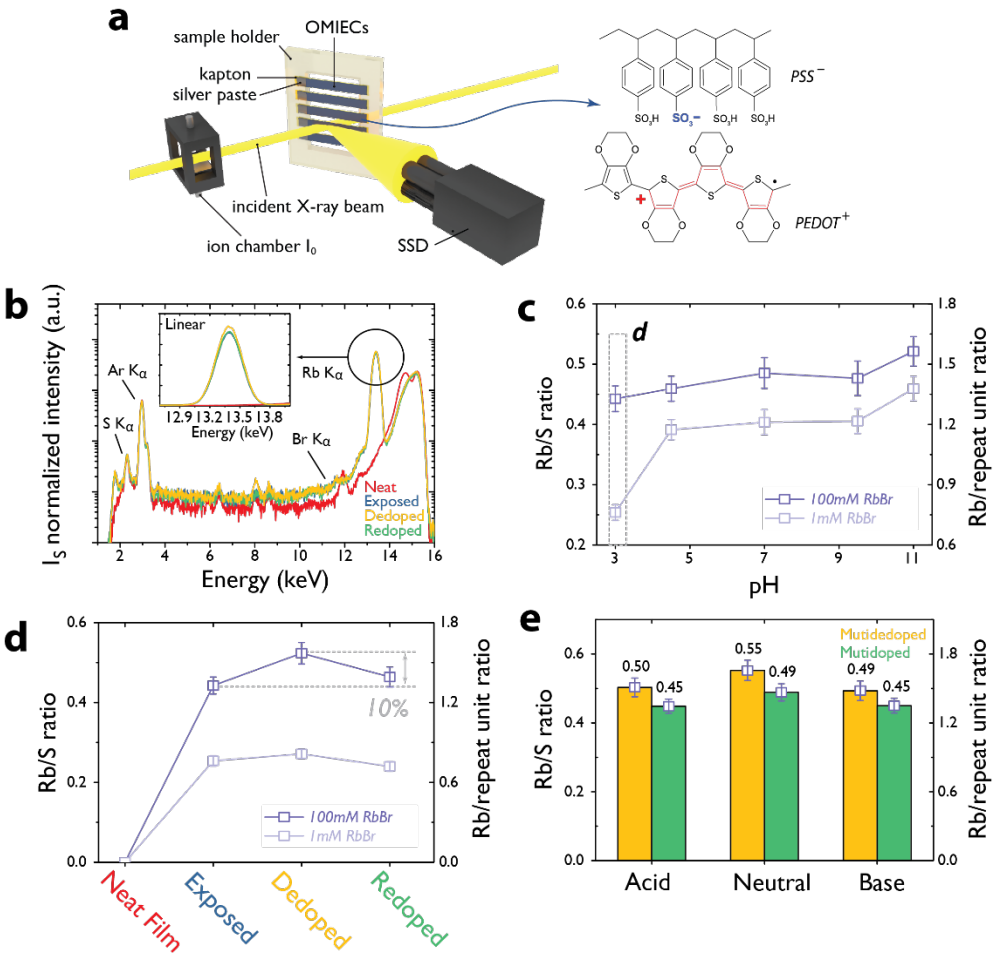

Figure 1 a) ex situ XRF setup and the structure of model OMIEC material, PEDOT:PSS; b) XRF spectra for EG/GOPS-PEDOT:PSS exposed and electrochemical cycled in 100mM at pH=7; c) Rb/S elemental ratio for EG/GOPS-PEDOT:PSS exposed to 1mM and 100mM RbBr aqueous electrolytes of different pH; d) Rb/S elemental ratio for EG/GOPS-PEDOT:PSS in different doping level electrochemical cycling in 1mM and 100mM at pH=3; e) Rb/S elemental ratio for EG/GOPS-PEDOT:PSS after multiple electrochemical cycling in acid (pH=3), neutral (pH=7) and basic (pH=11) conditions.

Results and Discussion

To measure elemental composition, ex situ XRF (**Figure 1a**) and XPS were performed on OMIECs exposed to and electrochemically cycled in aqueous electrolyte. Due to the limited path length of photoexcited electrons, XPS is only sensitive to the sample surface. However, XRF has a bulk sensitivity (micron scale), which provides bulk compositional information in a non-destructive and fast manner.

Metal halide salts were prioritized as they better reflect the ions present in biotic environments. In particular, RbBr was chosen as both the anion and cation fluoresce at higher energy (>12 keV) avoiding fluorescence overlap from ambient Ar (**Figure 1b**) and excessive photon absorption, which allows XRF measurements to be carried out under ambient conditions. These considerations are especially important when looking towards future in-situ/operando application of XRF measurements. In evaluating the generality of monovalent metal halide salts, OECTs employing aqueous 100 mM RbBr preformed nearly identically to the more commonly employed NaCl electrolytes at equivalent concentrations.[31] In addition, XPS performed on both RbBr and NaCl exposed samples revealed similar ion uptake, implying RbBr as a suitable approximation of other monovalent metal halide salts (**Figure S1**).

Compositional calibration curves were established by measuring the XRF spectra of a series of thiourea/RbBr mixture films with known S, Rb, and Br composition (**Figure S2a**). Calibration samples were spin coated on the same substrates as the OMIEC samples to avoid introducing new fluorescence that would complicate comparisons. Using these calibration data, XRF peak area ratios were converted into quantitative elemental compositions (**Figure S2b**).

First investigated was the benchmark OMIEC, PEDOT:PSS (structure in **Figure 1a**), prepared and cast using a commonly reported recipe containing ethylene glycol (EG) and (3-glycidyloxypropyl)trimethoxysilane (GOPS). EG functions as a processing additive known to drive PEDOT and PSS phase segregation yielding a morphology conducive to electronic transport,[26, 32-34] while GOPS is used as a crosslinker, activated by an ambient "hard-bake", to impart stability to the thin film and prevent film delamination or redispersion.[35, 36] The PEDOT:PSS itself consists of a water suspension of PEDOT templated upon an excess of PSS. A fraction of PSS^- anions serve as dopants, stabilizing positive charge carriers (holes) on the PEDOT backbone. Excess PSS^- anions are charge balanced with protons or cations. As supplied,

the commercial PEDOT:PSS employed was in the acid form (PSSH) with protons counterbalancing the remaining excess PSS^-.

The PEDOT:PSS water suspension was blended with 5% EG, 1% GOPS and 0.1% dodecylbenzenesulfonic acid (DBSA). The suspension was spin coated on Kapton films that were precleaned with acetone and iso-propanol. As cast EG/GOPS-PEDOT:PSS films contained a 1:2.0 thiophene sulfur to sulfonate sulfur ratio (as determined by XPS, see **Figure S1a&d**), in line with previous reports (1: 2.2-2.5).[10, 37] Considering that PEDOT:PSS prefers a doped state with a hole density of approximately one hole per three ethylenedioxythiophene (EDOT) repeat units,[38-41] roughly 83% of the sulfonates are excess, not functioning as dopants.

Ex situ XRF revealed that when exposed to RbBr electrolyte, EG/GOPS-PEDOT:PSS films underwent a large proton-cation exchange, with Rb^+ supplanting H^+ within the film. The equilibrium between proton and cation counterbalancing excess sulfonates was weakly dependent on electrolyte concentration and pH, showing significant differences only at the pH extremes and low metal halide concentration (**Figure 1c**). Thus, PSS^- functioned as a buffer, minimizing the effect of electrolyte concentration and pH on OMIEC composition, except for high pH (11) conditions and the combined low pH (3) low salt concentration (1 mM RbBr) condition. In the initially exposed low pH (3) and low salt concentration (1 mM RbBr) conditions, where electrolyte proton and Rb^+ concentrations are equivalent, there is likely equal parts Rb^+ and protons within the film. For neutral electrolyte solutions near biologically relevant salt concentrations (100 mM), the Rb^+ concentration within the film effectively supplants the entire disassociated proton concentration.

Initial cycles for some pH and electrolyte concentration conditions presented smaller than expected modulation of the cation concentrations, indicating a significant role of proton transport in initial film doping and dedoping. However, repetitive cycling appeared to break in the films and drive them towards a reversible equilibrium with the electrolyte that was dominated by metal cation transport. These multiple cycling experiments revealed a stabilized ~10% difference in Rb^+ concentration between the doped (0 V vs Ag/AgCl) and dedoped (-0.6 V vs Ag/AgCl) states (**Figure 1d**) across different pHs. While -0.6 V vs Ag/AgCl is not rigorously dedoped (zero electronic charge carrier density), it is sufficient to recover the majority of the neutral PEDOT species and arrive at the dedoped microstructure.[42] Potentials necessary to drive PEDOT:PSS to

the fully neutral state result in significant faradaic currents due to electrolyte breakdown or polymer degradation,[10, 43-45] and thus were avoided. When cycling from 0 to -0.6 V vs Ag/AgCl, for the neutral 100 mM RbBr condition, this represents a modulation of ~0.2 Rb^+ per ethylenedioxythiophene (EDOT) repeat unit. Given the presumed total doped hole density of ~0.33, this indicated much of the modulation in hole density is achieved through modulation of Rb^+ dopant density, though some minority proton contribution cannot be ruled out. The cation composition is reversible during multiple cycles of charging and discharging (**Figure 1e**). The Rb/S ratio increased slightly to 0.55 after multiple cycles in the dedoped state and 0.49 in the doped state.

Across electrolyte concentration and pH, Br^- anions were rigorously excluded to levels below the detection limit (<0.001 Br^- per EDOT repeat unit) due to Donnan exclusion arising from the fixed anionic charge of the excess PSS polyelectrolyte. This empirically validates the assumptions no mobile anion contribution implicit to previous PEDOT:PSS EQCM studies.[10, 35, 46, 47] However, in previous works the cation concentration was not measured directly but calculated from the charging currents, thus any faradaic side reactions not contributing to hole carrier density undermined the accuracy of the derived cation concentration within the OMIEC film.

To attend to this complication, EQCM was carried out to compliment these XRF studies and allow a complete mass and charge balance of the OMIEC films. Assuming a density of 1.0g/cm^3 and knowing the modulated cation concentration through XRF, the contribution to the mass change due to uptake of water molecules was calculated. The number of cations (injected/expelled) during cycling as quantified by XRF (**Figure 1e**) was used in the mass balance quantified by EQCM (**Figure S3a**) to calculate the amount of water that accompanies cation (injected/expelled). The combined experiments here indicate that on average ~11.6 H_2O molecules accompany each Na^+ cation injected/expelled in to EG/GOPS-PEDOT:PSS. This is nearly three times the estimated accompanying water molecules previously reported using solely EQCM methods where the cation flux was equated with measured electrical current. This highlights the overestimate of cation content that can occur when measured currents are assumed to be purely cation flux. This ignores faradaic reactions that result in direct charge transfer, which can be especially large in aqueous environments in the presence of oxygen.[48, 49] These

faradaic reactions arising from PEDOT based materials can in fact be harnessed as reported in PEDOT-based electrocatalysts.[48, 50-52]

Our calculated cation-associated water content is more in line with near ambient pressure XPS measurements of water content (~8-10 per cation) associated with a metal halide counterbalanced PSS^- functional group.[53] It is intuitively reasonable that our cation-associated water uptake of a PSS containing film in contact with liquid electrolyte would exceed sorption measurements of PSS films in 100% relative humidity environments (but not in contact with liquid water). The experiments reported here indicate that cation transport into the film is accompanied by more than a single hydration shell.[54, 55]

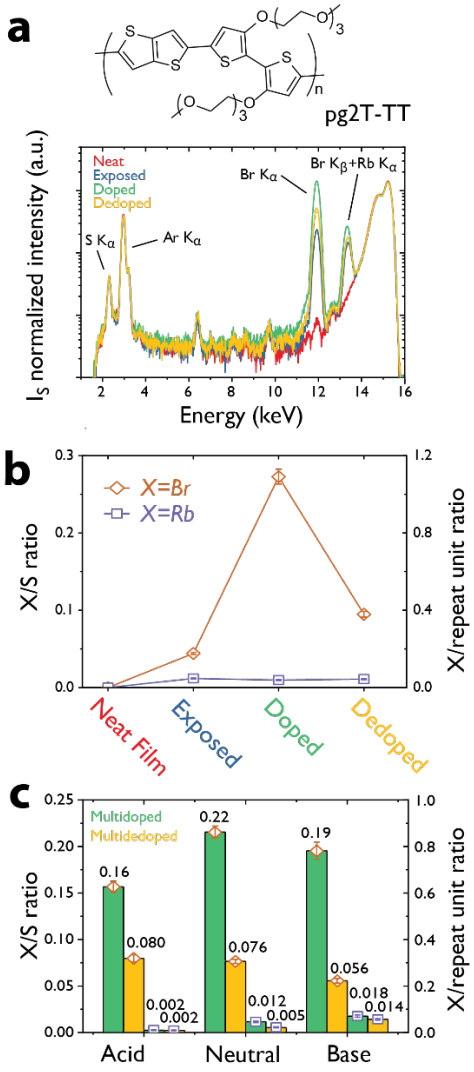

Figure 2 a) XRF spectra for pg2T-TT exposed and electrochemical cycled in 100mM at pH=7; b) Br (brown diamond) and Rb (violet square) to S ratio of pg2T-TT in different electrochemical doping level; c) Rb (brown diamond) or Br (violet square) to S elemental ratio for pg2T-TT after multiple electrochemical cycling (the doped states filled with green and the dedoped states filled with yellow) in acid (pH=3), neutral (pH=7) and basic (pH=11) conditions.

While EG/GOPS-PEDOT:PSS is a prototypical conjugated polymer/polyelectrolyte composite OMIEC, polythiophenes with oligoethylene glycol side chains have become increasingly popular conjugated polymer electrolyte OMIECs.[56-58] In particular, pg2T-TT (**Figure 2a**) has been investigated for a variety of applications.[17, 56, 59, 60] Lacking any fixed ionic charge, Donnan exclusion is not expected in pg2T-TT, and both cations and anions appeared in the XRF spectra (**Figure 2a&b**). The florescence spectra at 200eV below the Rb absorption edge were collected to deconvolute and Rb K_α peaks from the overlapped Br K_β peaks (**Figure S4a**). XRF following electrolyte exposure revealed the passive uptake of both anions and cations, 0.16 Br^- and 0.04 Rb^+ per repeat unit (**Figure 2b**). This was in agreement with previous qualitative measurements of ion uptake in contact with ionic liquid electrolytes.[17] However, here the calibrated quantitative measure of individual ion concentrations revealed that anions and cations did not uptake in equal amount, indicating extensive passive doping of pg2T-TT. This is attributed to its relatively shallow HOMO allowing for rather efficient doping via ambient oxygen.[48] The passive uptake of Rb^+ led to a cation concentration that subtly varied with doping (oxidation) state.

Initial cycling between the doped state (+0.5V vs Ag/AgCl) and dedoped state (-0.2V vs Ag/AgCl) greatly modulated the Br^- anion concentration, though even when a reductive electrochemical potential was applied a large excess of anions (uncompensated by cations) remained. Unlike the PEDOT:PSS cycling, it should be noted here that the reductive potentials applied were sufficient to fully dedope the polymer. These initial phenomena persisted upon multiple cycles, equilibrating to seemingly permanent presence of 0.021 charged balanced anions and cations per repeat unit, and a further uncompensated 0.29 excess anions per repeat unit (**Figure 2c** and the second right column in **Figure S4b**). Due to the energetic favorability of charge neutrality, these seemingly uncompensated excess anions are presumably counterbalanced by localized positive charge on the polymer backbone (i.e. trapped electronic

charge). This measured trapping level (~10^{20} cm^{-3}) is much higher than expected defect levels in polythiophenes (10^{13} – 10^{19} cm^{-3}).[61-66] Thus it is surmised that electrochemical cycling of the films does not simply passivate existing trapped electronic charge with excess anions, but induces many additional trap sites as well.

From the dedoped to doped state the concentration of charge balanced anions and cations roughly doubled to 0.048 anion-cation pairs per repeat unit, and the concentration of uncompensated anion dopants nearly tripled to 0.82 per repeat unit (the second left column in **Figure S4b**). The presence of charged balanced ions appears to represent a permanent population due to passive electrolyte swelling of the film. The increase in charge balanced anion-cation pairs in the doped state reflects an increase miscibility of the polymer and electrolyte when the polymer is charged.

Interestingly, excess cation accumulation in the dedoped state was not observed. Instead, cation composition in the dedoped state was diminished compared to the doped state. This stood in contrast to previous reports where a dedoping occurs by both anion expulsion and cation insertion to counterbalance remaining anion dopants in both conjugated[16] and radical OMIECs.[15] It must be noted that these previous studies either did not employ metal halide salts, or in the case of radical polymers, employed non-aqueous electrolytes. The absence of cation accumulation highlights that aqueous metal halide transport in OMIEC based bioelectronic devices can deviate significantly from systems employing salts and solvents more common in energy storage devices. Here, cations do not contribute to the doping/dedoping process, but simply participate through passive electrolyte swelling of the pg2T-TT film, the miscibility of which depends on the film's charged state.

Lacking any excess polyelectrolyte to act as a buffer (such as in the case of PEDOT:PSS), the ion composition of pg2T-TT was found to be dependent on electrolyte concentration and pH (**Figure S5**). At neutral pH, anion concentration in the polymer was positively correlated with electrolyte concentration at all states (exposed/doped/dedoped). The observed dependence of anion concentration in the polymer upon electrolyte concentration was larger than would be expected from a shift in doping state due to a Nernst-like shift in electrochemical potential (59 mV shift per decade of electrolyte concentration). Instead, a ~55% drop in dopant anion concentration was observed when decreasing electrolyte concentration from 100 to 10 mM, and a

further ~40% drop from 10 to 1 mM (**Figure S5a**). The persistent (trapped) anion concentration within the rigorously dedoped film was also dependent on electrolyte concentration. The trapped anions were in an apparent equilibrium with the contacting aqueous electrolyte, undergoing a 30-40% decrease with each ten-fold decrease in electrolyte concentration (**Figure S5a**).

Cation concentration was positively correlated with pH, rising from 0.008 (0.008) Rb^+ per repeat unit in acidic conditions to 0.072 (0.056) Rb^+ per repeat unit in basic conditions in the doped (dedoped) state (**Figure S4b**). This reflects the competition in acidic solution between the Rb^+ and proton counterbalancing the halide anion, and in the case of basic solutions, counterbalancing the hydroxide anion. The trapped anion concentration shows an opposite trend with pH, falling from 0.31 trapped excess Br^- per repeat unit in acidic conditions to 0.16 trapped excess Br^- per repeat unit in basic conditions (**Figure S4b**). This likely reflects the effect of protonation of the polymer on both free carrier and defect/trap density.[67-70]

The modulated Br^- concentration (difference between doped and dedoped state) was nominally identical in neutral and basic conditions (0.53 and 0.54 Br^- dopants per repeat unit, respectively, see **Figure S4b**). This indicated that basic pH seemed not to effect the doping/dedoping process. However, the acid condition displayed a diminished degree of Br^- dopant modulation of only 0.31 Br^- dopants per repeat unit, indicating the protonation of thiophene rings may disrupt the doping/dedoping process.[67]

Summarizing the contrast between EG/GOPS-PEDOT:PSS and pg2T-TT, EG/GOPS-PEDOT:PSS undergoes an initial exchange of protons in the film with metal cations from the electrolyte. The excess polyelectrolyte in EG/GOPS-PEDOT:PSS simplifies the composition situation by Donnan excluding uptake of mobile anions and buffering the film against pH and electrolyte concentration, such that doping/dedoping involves a fairly consistent modulation of >0.2 cations per EDOT repeat unit. However, this cation modulation brings with it a large flux of water molecules in/out of the film. Conversely, pg2T-TT undergoes passive electrolyte uptake (water and anion-cation pairs) and passive doping. Electrochemical cycling accumulates a remarkably high concentration of excess anions that apparently balance/trap electronic charge in the polymer. Lacking fixed charge, pg2T-TT is unbuffered, and the resulting film composition is highly sensitive to electrolyte concentration and pH.

Having quantified the ion composition of prototypical polyelectrolyte:conjugated polymer and conjugated polymer electrolyte OMIECs, we turned to the top performing OMIEC, sulfuric acid crystallized PEDOT:PSS (crys-PEDOT:PSS).[71, 72] Post treatment of PEDOT:PSS films with concentrated sulfuric acid removes excess PSS and drives the nanofibrillar crystallization of the remaining PEDOT:PSS.[73] Treatment with 95% sulfuric acid reduces the PSS-to-PEDOT ratio from ~2:1 to 0.41:1, **Figure S6**, in line with previous reports.[72-74]

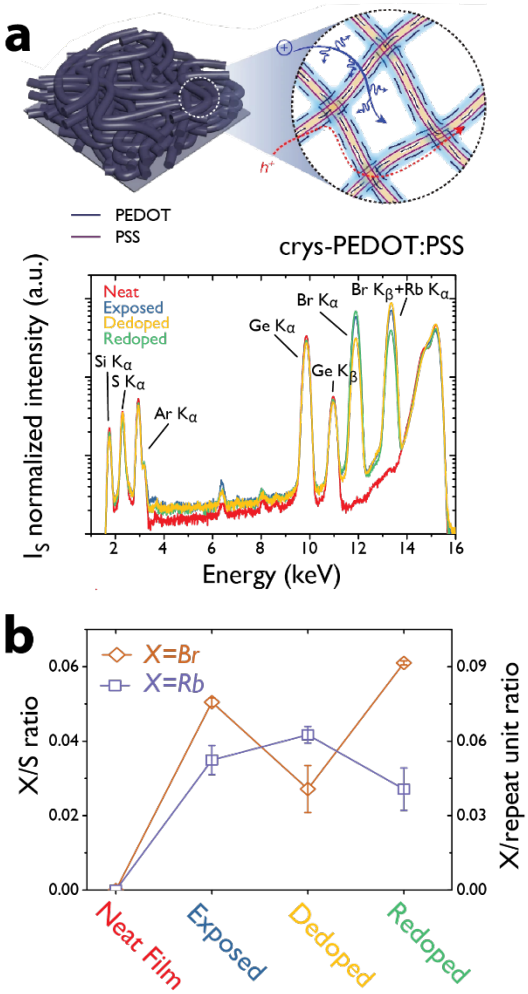

Figure 3 a) XRF spectra for crys-PEDOT:PSS (PEDOT:PSS treated with 95% sulfuric acid) exposed and electrochemical cycled in 100mM at pH=7; b) Br (brown diamond) and Rb (violet square) to S ratio of 95% sulfuric acid crys-PEDOT:PSS in different electrochemical doping level.

We have previously reported the XRF determined composition of 95% sulfuric acid crys-PEDOT:PSS in the doped and dedoped states (**Figure 3**).[75] Quantitative comparison of crys-PEDOT composition with EG/GOPS-PEDOT:PSS and pg2T-TT are complicated due to substrate effects (thickness dependent Si absorption of S fluorescence leading to likely underestimate of relative Rb and Br concentrations). Qualitatively, crys-PEDOT:PSS exposed, doped, and dedoped composition is radically different from EG/GOPS-PEDOT:PSS as the removal of excess PSS during acid treatment suppresses the effect of Donnan exclusion (**Figure 3a**). Thus, both cations and anions are free to transport in and out the film, and resulting Br^- concentrations are on the same order as Rb^+ concentrations.

Electrolyte exposure results in the uptake of both anions and cations, with anions in the excess. Whereas, EG/GOPS-PEDOT:PSS displayed solely Rb^+ uptake representing proton-cation exchange. In 95% sulfuric acid treated crys-PEDOT:PSS initial proton concentration is minimal as effectively all PSS sulfonates are dopants counterbalancing positive electronic charge on PEDOT, thus no significant proton-cation exchange occurs upon exposure. Instead, in the absence of Donnan exclusion charge balanced anions and cations diffuse into the film (**Figure 3b**). Further, excess anions accumulate as the equilibrium doping level in neutral aqueous environments is higher than in the sulfuric acid processing conditions, resulting in an ~30% excess of Br^- with respect to Rb^+.

When electrochemically dedoped (-0.6 V vs Ag/AgCl), the electronic charge density on the PEDOT is decreased both through the removal of mobile Br^- dopants, and the accumulation of excess Rb^+ cations that counterbalance fixed PSS- dopants, supplanting positive electronic charge (**Figure 3b**). The resulting dedoped composition has a ~37% excess Rb^+ with respect to Br^-. Finally, when electrochemically redoped back to a high oxidation state (+0.6 V vs Ag/AgCl), the Br^- concentration climbs and the Rb^+ concentration drops (**Figure 3b**). The resulting redoped composition has a ~55% excess Br^- with respect to Rb^+, with the excess Br^- functioning as dopants, stabilizing positive electronic charge on PEDOT.

The difference in ion uptake between EG/GOPS-PEDOT:PSS and crys-PEDOT:PSS was also reflected in the EQCM data (**Figure S3b**). EG/GOPS-PEDOT:PSS displayed mass uptake during dedoping to a low oxidation state (-0.7 V vs Ag/AgCl) and mass decrease when doping to a high

oxidation state (+0.5 V vs Ag/AgCl) with respect to the equilibrium oxidation state (~0.1 V vs Ag/AgCl), consistent with solely cation transport. In comparison, crys-PEDOT:PSS shows a mass increase both upon dedoping and doping to the low (-0.7 V vs Ag/AgCl) and high oxidation states (+0.5 V vs Ag/AgCl), respectively, indicating a more complicated transport environment with both mobile anions and cations contributing. Normalizing the EQCM mass changes by film thickness it becomes apparent that the mass increase (+14%) accompanying dedoping to a low oxidation state (-0.7 V vs Ag/AgCl) and mass decrease (-11-12%) accompanying redoping to the equilibrium oxidation state (~0.1 V vs Ag/AgCl), were nearly identical for both EG/GOPS-PEDOT:PSS and crys-PEDOT:PSS. When further doping to a high oxidation state (+0.5 V vs Ag/AgCl), crys-PEDOT:PSS displayed a 3.4% mass increase, compared with 8.3% mass decrease in EG/GOPS-PEDOT:PSS.

Considering crys-PEDOT:PSS ion concentration changes alone, upon doping to a high oxidation state (large anion concentration increase, moderate cation concentration decrease), a mass increase is expected (opposite to EG/GOPS-PEDOT:PSS, large cation decreases only) and is observed with EQCM. Though considering crys-PEDOT:PSS ion concentration changes alone upon dedoping to a low oxidation state (large anion concentration decrease, moderate cation concentration increase), a slight mass decrease would be expected. Instead, a moderate mass increase was observed indicating enhanced water uptake accounting for this discrepancy. Thus, the amount of water accompanying ion transport cannot be presumed to be constant across oxidation state.

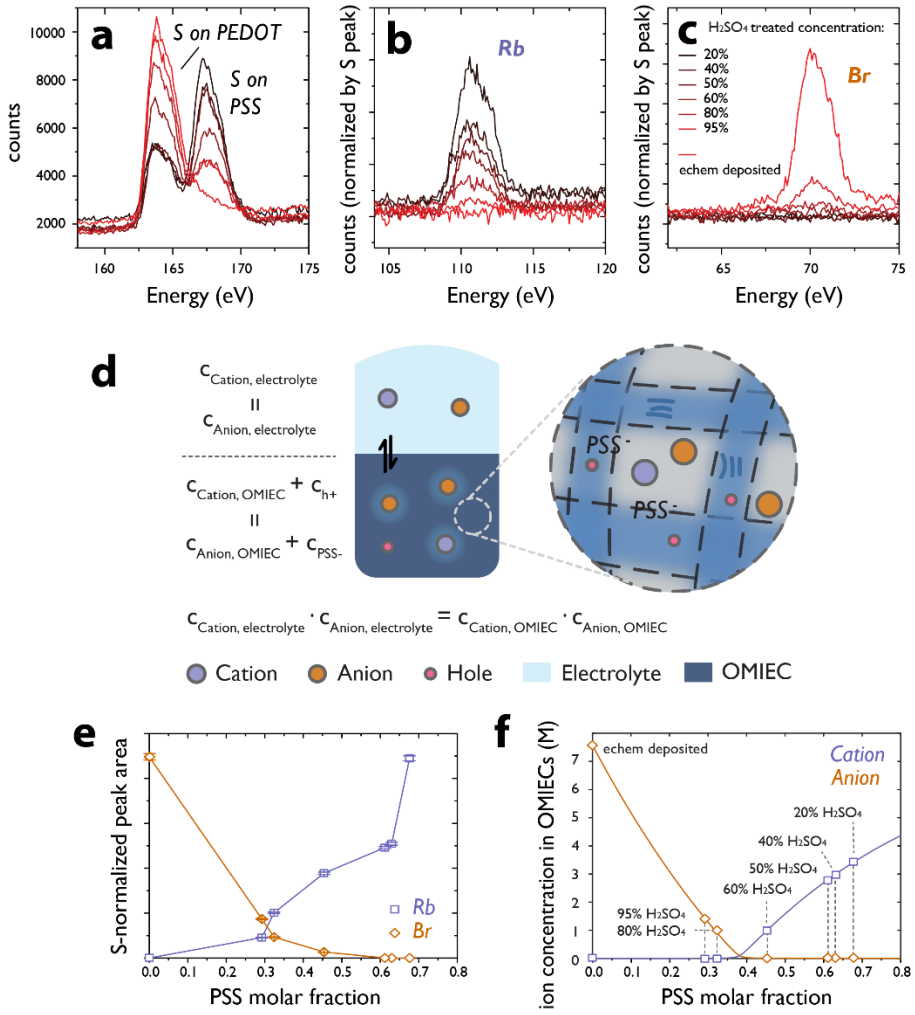

Figure 4 XPS result of the a) sulfur, b) sulfur normalized rubidium and c) sulfur normalized bromine peaks in PEDOT:PSS treated with sulfuric acid of different concentration (from 20%-95%, black to dark red) and electrochemically deposited PEDOT (red); d) diagram for the Donnan model; e) ion peak fits extracted from the XPS experimental result; f) the calculated result from the Donnan model, plotted with the PSS molar content of each material.

In sulfuric acid treated crys-PEDOT:PSS, the strength of acid during crystallization allows the control of the excess PSS^- concentration, i.e. allows the tuning of fixed cationic charge within the OMIEC. Leveraging this, we investigated the effect of fixed charge upon ion uptake with XPS compositional analysis on electrolyte exposed PEDOT:PSS previously treated with sulfuric acid of different concentration (**Figure S6**). XPS allowed the simultaneous measure of the

PSS:PEDOT ratio and the qualitative ion concentration changes, while XRF was carried out to confirm the ion concentration trends through the bulk.

The ratio of sulfonate to thiophene sulfur in the acid treated PEDOT:PSS decreased from 2.08:1 to 0.41:1 as the acid treatment concentration increased from 20% to 95% sulfuric acid (**Figure 4a**). This reflected a modulation of PSS content from 0.68 down to 0.29 PSS mol fraction (with respect to combined PSS and PEDOT content). Electrochemical deposited PEDOT film (soaked in 100mM RbBr solution for ion exchange) was used as a PSS-free (0.0 PSS mol fraction) standard, lacking any fixed cationic charge.

XPS revealed the concentration of cations in the polymer films to continually decrease with decreasing PSS mol fraction, with no Rb^+ cations present in the 0.0 PSS mol fraction electrodeposited PEDOT film (**Figure 4b**). The presence of Br^- anions decreased with increasing PSS mol fraction and was suppressed to concentrations below the detection limit above 0.6 PSS mol fraction (>50% sulfuric acid treatment concentration, **Figure 4c**), representing the threshold beyond which fixed cationic charge density was sufficient to exclude mobile anions. These trends were further confirmed with benchtop XRF measurements (**Figure S7a&b**), with some variation in Rb^+ concentration at high PSS mol fraction.

A Donnan model was established to semi-quantify the trend of passive ion uptake in different polyelectrolyte (PSS^-) content (see **SI: Gibbs-Donnan Model in PEDOT:PSS**). Shown in **Figure 4d**, the whole system was simplified as two phases: aqueous electrolyte with only mobile anion/cations and OMIECs with extra fixed charges (holes and PSS^-) on the crystalline fiber. Ion concentration inside the OMIEC can be described by the following Donnan-Gibbs equation:

$$c_{Cation,OMIEC} \cdot c_{Anion,OMIEC} = {c_s}^2 \qquad (1)$$

Where $c_{X,OMIEC}$ represents the ion concentration in OMIEC and c_s represents the ion concentration in aqueous electrolyte. By assuming a suitable hole concentration,[41, 73, 74] the specific ion concentration in OMIEC can be solved by combining the charge-neutral condition with the Donnan-Gibbs equation (**Equation 1**, also **S8**), shown in **Figure 4e**. Despite the simplicity of the model, the ion concentrations extracted from XPS (**Figure 4f**) and XRF (**Figure S7c**) were in good agreement with the prediction from the Donnan model, capturing the suppression of Br concentration above an intermediate PSS mol fraction (Donnan exclusion of

anions). While the exact value of this PSS mol fraction threshold for complete Donnan exclusion in the model was sensitive to assumed hole concentration, the crossover of cation concentration overtaking anion concentration occurs in both the model and the measured data just above a 0.3 mol fraction PSS content.

As this model only considers the Donnan equilibrium of salt ions between the two phases, it does not account for the evolution of film morphology with increasing acid treatment concentration. With concentrated sulfuric acid treatment, the resulting nano fibrillar structure introduces void space within the film, where charge balanced anion-cation pairs (along with water) are able to reside. This likely gives rise to the observed non-zero cation concentration at lower PSS mol fraction. Further, ions entering the crystalline nano fibrillar structures may themselves be in thermodynamic equilibrium with the ions in the voids within the film (in addition to the external electrolyte). Also, ion trapping within the film may also occur to give an increased ionic content.

Whether considering the voids and nanofibrillar domains within crys-PEDOT:PSS,[72, 73] the PEDOT-rich versus PSS-rich domains within EG/GOPS-PEDOT:PSS,[26] or the crystalline and amorphous domains in pg2T-TT,[56] the distribution of ions throughout OMIECs is not necessarily homogenous. In the case of EG/GOPS-PEDOT:PSS, the meso-scale structure is a mixture of PEDOT-rich and PSS-rich domains.[26] Thus, passive cation-proton exchange is expected to lead to higher metal cation concentrations within the PSS-rich domains than the PEDOT-rich domains. Semi-crystalline pg2T-TT is presumed to present ordered/crystalline domains embedded in an amorphous matrix, similar to well-studied alkyl-side chain polythiophenes.[76-78] Spectroscopic studies on closely related alkyl-sidechain materials have been interpreted as indicating a potential-dependent differential distribution of dopant ions between the amorphous and crystalline regions.[79] Thus, to further understand the distribution of ions in OMIEC films, we performed ex situ GISAXS experiments collecting 2-D small angle scattering patterns from films as prepared (neat), after electrolyte exposure, and after electrochemical (re/de)-doping. In GISAXS, the changes in feature positions indicate a change in mesoscale structure on exposure/electrochemical biasing, where as a change in feature intensity decay would be an indicator of changes in electron density associated with ionic/water distributions.

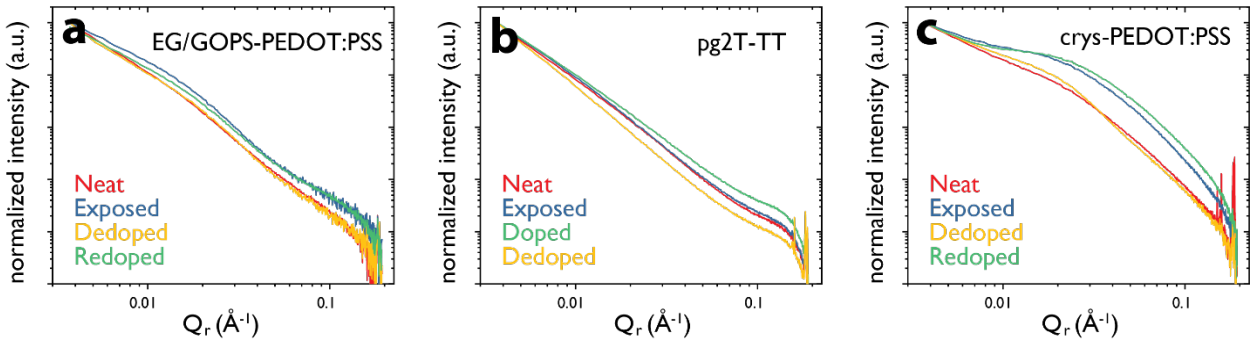

Figure 5 the in-plane (q_r) linecut of GISAXS patterns in Yoneda region of a) EG/GOPS-PEDOT:PSS, b) pg2T-TT and c) crys-PEDOT:PSS in different doping level.

2-D ex situ GISAXS patterns were collected for EG/GOPS-PEDOT:PSS films neat/as cast, electrolyte exposed, electrochemically dedoped (-0.6 V vs Ag/AgCl), and electrochemically redoped to a roughly equilibrium oxidation state (0.0 V vs Ag/AgCl) (**Figure S8**). Line-cuts from all the films conditions displayed a similar broad scattering feature between 0.01 and 0.03 $Å^{-1}$ (**Figure 5a**), indicating that mesoscale structure (phase separation of PEDOT-rich and PSS-rich domains) is essentially constant due to high level of crosslinking, with a domain length-scale in keeping with previous investigations.[26]

With ex situ exposed and biased films, the changes in small angle scattering intensity are ascribed to larger changes in cation concentration within the PEDOT-rich domains compared to the PSS-rich matrix.[26] The exposed (having undergone proton-cation exchange) and redoped line cuts were nominally identical, which was intuitive as they should both have same cation concentration and distribution. The neat and dedoped line-cuts were nominally identical with each other, and distinct from the exposed and redoped line cuts, with a suppression of the main scattering feature. This reflects a diminished electron density contrast between the PSS-rich and PEDOT-rich domains due to the minimal effect of protons in the cation-free neat film, and the decreased differential cation concentration between the domains in the dedoped samples, as cations displace holes in the PEDOT-rich domains.

GISAXS patterns of pg2T-TT neat, ex situ electrolyte exposed, dedoped (-0.2 V vs Ag/AgCl), and redoped (+0.5 V vs Ag/AgCl) films were also collected (**Figure S9**). Line-cuts from the neat and electrolyte exposed films were nominally identical (**Figure 5b**), implying no meso-scale

disruption/reordering and a uniform distribution of passively incorporated ions. This stands in contrast to analogous alkyl sidechain polythiophenes exposed to ionic liquid electrolytes, where ions are presumed to preferentially enter the amorphous domains.[79] Here, a uniform ion uptake in both amorphous and crystalline domains is in keeping with the large lamellar expansions in pg2T-TT upon electrolyte exposure seen with in situ GIWAXS.[80] It is difficult to rationalize 60% lamellar expansion not reflecting significant ion uptake into the intra-lamellar regions of crystalline domains. Compared to the neat and exposed films, line-cuts from ex situ dedoped films displayed a subtle slope increase and intensity decrease, while line-cuts from ex situ redoped films displayed a subtle slope decrease and intensity increase. The relatively minimal scattering differences across conditions implies that passive ion uptake, and potential dependent (de)doping results in relatively uniform changes in ion density within the amorphous and crystalline domains of pg2T-TT in aqueous metal halide electrolytes.

In both EG/GOPS-PEDOT:PSS and pg2T-TT, the differences in GISAXS patterns across conditions indicate small morphological changes relative to the meso-scale changes that occur in related conjugated polymer systems during co-deposition,[81] in response to changes in humidity,[82] and operation in a thermoelectric[25] or photovoltaic devices.[83]

In contrast to the subtle changes in small angle scattering in EG/GOPS-PEDOT:PSS and pg2T-TT, crys-PEDOT:PSS showed much larger differences in small angle scattering between ex situ conditions (**Figure 5c**, **Figure 6a-d**). In this case, the conditions were neat (as prepared, **Figure 6a**), electrolyte exposed (**Figure 6b**), dedoped (-0.6 V vs Ag/AgCl, **Figure 6c**), and redoped to a high oxidation state (+0.6 V vs Ag/AgCl, **Figure 6d**). As discussed above, sulfuric acid treatment of PEDOT:PSS removed excess PSS and drove the formation of a crystallized nanofibrillar structure. Thus, the anticipated possible effects of ex situ electrolyte exposure and electrochemical (de)doping are differential accumulation of ions within the crystalline nanofibers and voids, and swelling of the crystalline nanofibers.

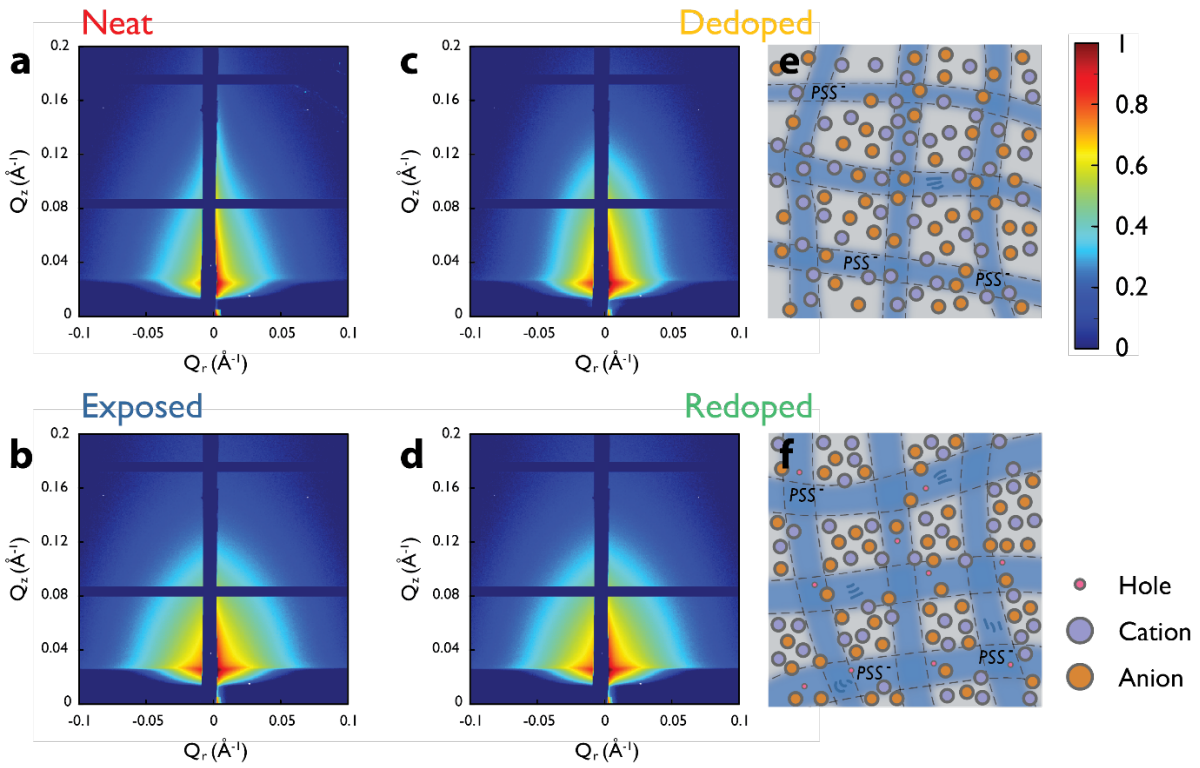

Figure 6 GISAXS patterns for crys-PEDOT:PSS in a) neat film; b) exposed in 100mM RbBr solution at pH=7; c) dedoped at -0.6V vs Ag/AgCl in 100mM RbBr solution at pH=7; d) redoped to a high oxidation state at +0.6V vs Ag/AgCl in 100mM RbBr solution at pH=7; e) schemes for ion distribution in the neat, dedoped states and f) exposed, redoped states.

Neat film GISAXS line-cuts displayed a pronounced shoulder around 0.02 $Å^{-1}$ (**Figure 5c**). This feature was enhanced and shifted to higher q-vector upon electrolyte exposure, diminished upon dedoping, and enhanced once again when redoped to a high oxidation state, all in keeping with previously reported low q-vector in situ GIWAXS scattering behavior.[42] The normalized intensity contrast is significantly enhanced when crys-PEDOT:PSS is in the doped state (both electrolyte exposed and redoped states, **Figure 6b&d**), implying a non-uniform ion distribution. With respect to the neat (as prepared) films, in-plane line-cuts from exposed and redoped film GISAXS scattering patterns both displayed an increase in intensity of the scattering feature and a shift to higher q-vector (**Figure 5c**). The intensity increase due to exposure is ascribed to larger electron density contrast between the crystalline nanofibrillar domains and the inter-fibrillar voids/domains arising from inhomogeneous uptake of ions into the film (**Figure 6f**). From ex

situ XRF, it is apparent that significant amount of charge balanced anion-cation pairs enters the film, which presumably reside in inter-fibrillar voids/domains. Additionally, ex situ XRF revealed that excess anions also enter the film, (as the equilibrium degree of doping in pH neutral electrolyte is higher than as prepared), and these dopant anions are expected to reside within the nanofibrils to compensate the enhanced hole density. Thus we tentatively interprets the shift to higher q-vector as reflecting a shrinking of the inter-fibrillar voids/domains as the crystalline nanofibrils expand.

With respect to the exposed and redoped films, in-plane line-cuts from dedoped film GISAXS scattering patterns displayed a decrease in intensity of the scattering feature and a shift to higher q-vector, bringing it more in line with the as prepared scattering data (**Figure 5c**). The intensity decrease is ascribed to suppression of the electron density contrast between the crystalline nanofibrillar domains and the inter-fibrillar voids/domains due to the ion reorganization (cation accumulation within the nanofibrils) that accompanies dedoping, while the shift to higher q-vector as reflects an expansion of the inter-fibrillar voids/domains as the nanofibrils contract (**Figure 6e**).

A Guinier-style analysis of the line-cuts was carried out to provide a semi-quantitative analysis of the relative mesoscale changes (**Figure S10**). From the Guinier-style analysis of the particle size distribution a square weighted average characteristic length scale was obtained (**Table S1**). Again, this length scale is interpreted as representing the size of inter-fibrillar voids/domains embedded in a nanofibrillar mesh. In keeping with our above qualitative analysis, the as cast (neat) and dedoped samples gave similar characteristic length scales, 128 and 132 Å, respectively. The exposed and redoped samples were likewise similar, with characteristic length scales of 78.0 and 66.7 Å, respectively. The ~50-65 Å difference between exposed/redoped and neat/dedoped is ascribed to a contraction of the inter-fibrillar void/domain. This inter-fibrillar void/domain contraction is inversely correlated with a crystallite expansion (~12%) previously determined by in situ GIWAXS.[42] As the acid treatment produces highly crystalline nanofibrils, it is presumed that the nanofibrillar expansion is likely equivalent to the crystallite expansion.

It must be noted that ex situ GISAXS probes the dry “collapsed” structure, water (which by EQCM, contributes significantly to swelling) is for the large part absent from the films. What is interpreted in the ex situ films as an inter-fibrillar void/domain contraction may not maintain in

situ when the film is swollen with water as well as extra ions. This highlights the need for in situ/operando GISAXS for OMIECs, which is an ongoing effort.

Conclusion

In summary, we quantified the ionic composition of different species of p-type OMIEC after electrolyte exposure and electrochemical cycling. Among them, the presence of polyelectrolyte in OMIEC significantly affects the ionic species involved in the electrochemical cycle. The polyelectrolyte functioned as a buffer and minimized the effect of electrolyte concentration and pH on the changes in OMIEC composition. Specifically, the negatively charged polyelectrolyte PSS^- prevents mobile anions from entering the polymer due to Donnan exclusion. The passive ion uptake under electrolyte exposure in PEDOT:PSS with different polyelectrolyte contents was simulated by an appropriate Donnan model. The amount of fixed charge controls the strength of Donnan exclusion and thus controls the ultimate film composition. We also analyzed the mesoscale structure and ion distribution using GISAXS, which shows mild ion segregation in the polymer blend EG/GOPS-PEDOT:PSS and little ion segregation in single-component OMIEC pg2T-TT during the electrochemical cycling. In the crys-PEDOT:PSS with a well-defined fibrillar crystalline structure, the doped state of the polymer shows a significant inhomogeneous ion distribution and a contraction of the inter-fibrillar void/domain.

Acknowledgements

R.W., B.P., and J.R. gratefully acknowledge support from the National Science Foundation Grant No. NSF DMR-1751308. The synchrotron XRF work was performed at the 5-BM-D beamline of the DuPont-Northwestern-Dow Collaborative Access Team (DND-CAT) located at Sector 5 of the Advanced Photon Source (APS). DND-CAT is supported by Northwestern University, The Dow Chemical Company, and DuPont de Nemours, Inc. GISAXS measurements were performed at beamline 8-ID-E of the APS. The APS is a U.S. Department of Energy (DOE) Office of Science User Facility operated for the DOE Office of Science by Argonne National Laboratory under Contract No. DE-AC02-06CH11357. This research used resources of the Advanced Photon Source; a U.S. Department of Energy (DOE) Office of Science User Facility

operated for the DOE Office of Science by Argonne National Laboratory under Contract No. DE-AC02-06CH11357. This work utilized the Keck-II facility of Northwestern University's NUANCE Center, supported by the Soft and Hybrid Nanotechnology Experimental (SHyNE) Resource (NSF ECCS-1542205), the Materials Research Science and Engineering Center (NSF DMR-1720139), the State of Illinois, and Northwestern University. Additionally, the Keck-II facility is partially supported by the International Institute for Nanotechnology (IIN); the Keck Foundation; and the State of Illinois, through the IIN. This work also utilized the IMSERC facility in Northwestern University. IMSERC is funded by NSF CHE-9871268 (1998) and Northwestern University.

Reference

1. C. Pitsalidis, A.-M. Pappa, A. J. Boys, Y. Fu, C.-M. Moysidou, D. Van Niekerk, J. Saez, A. Savva, D. Iandolo and R. M. Owens, *Chemical Reviews*, 2021.
2. M. Berggren, E. D. Głowacki, D. T. Simon, E. Stavrinidou and K. Tybrandt, *Chemical Reviews*, 2022, **122**, 4826-4846.
3. E. Manousiouthakis, J. Park, J. G. Hardy, J. Y. Lee and C. E. Schmidt, *Acta Biomaterialia*, 2021.
4. A. J. Petty, R. L. Keate, B. Jiang, G. A. Ameer and J. Rivnay, *Chemistry of Materials*, 2020, **32**, 4095-4115.
5. M. G. Sumdani, M. R. Islam, A. N. A. Yahaya and S. I. Safie, *Polymer Engineering & Science*, 2022, **62**, 269-303.
6. A. Malti, R. Brooke, X. Liu, D. Zhao, P. Andersson Ersman, M. Fahlman, M. P. Jonsson, M. Berggren and X. Crispin, *Journal of Materials Chemistry C*, 2016, **4**, 9680-9686.
7. Q. Zhang, C.-Y. Tsai, L.-J. Li and D.-J. Liaw, *Nature Communications*, 2019, **10**.
8. H. Ling, D. A. Koutsouras, S. Kazemzadeh, Y. Van De Burgt, F. Yan and P. Gkoupidenis, *Applied Physics Reviews*, 2020, **7**, 011307.
9. X. Ji, B. D. Paulsen, G. K. K. Chik, R. Wu, Y. Yin, P. K. L. Chan and J. Rivnay, *Nature Communications*, 2021, **12**.
10. A. Savva, S. Wustoni and S. Inal, *Journal of Materials Chemistry C*, 2018, **6**, 12023-12030.

11. A. Savva, C. Cendra, A. Giugni, B. Torre, J. Surgailis, D. Ohayon, A. Giovannitti, I. McCulloch, E. Di Fabrizio, A. Salleo, J. Rivnay and S. Inal, *Chemistry of Materials*, 2019, **31**, 927-937.
12. A. Savva, D. Ohayon, J. Surgailis, A. F. Paterson, T. C. Hidalgo, X. Chen, I. P. Maria, B. D. Paulsen, A. J. Petty, J. Rivnay, I. McCulloch and S. Inal, *Advanced Electronic Materials*, 2019, **5**, 1900249.
13. Y. Wang, A. Hamidi-Sakr, J. Surgailis, Y. Zhou, H. Liao, J. Chen, G. Zhu, Z. Li, S. Inal and W. Yue, *Journal of Materials Chemistry C*, 2021, **9**, 13338-13346.
14. A. A. Szumska, I. P. Maria, L. Q. Flagg, A. Savva, J. Surgailis, B. D. Paulsen, D. Moia, X. Chen, S. Griggs, J. T. Mefford, R. B. Rashid, A. Marks, S. Inal, D. S. Ginger, A. Giovannitti and J. Nelson, *Journal of the American Chemical Society*, 2021, **143**, 14795-14805.
15. S. Y. Wang, F. Li, A. D. Easley and J. L. Lutkenhaus, *Nat Mater*, 2019, **18**, 69-+.
16. L. Q. Flagg, C. G. Bischak, R. J. Quezada, J. W. Onorato, C. K. Luscombe and D. S. Ginger, *ACS Materials Letters*, 2020, **2**, 254-260.
17. T. J. Quill, G. Lecroy, A. Melianas, D. Rawlings, Q. Thiburce, R. Sheelamanthula, C. Cheng, Y. Tuchman, S. T. Keene, I. McCulloch, R. A. Segalman, M. L. Chabinyc and A. Salleo, *Advanced Functional Materials*, 2021.
18. B. D. Paulsen, K. Tybrandt, E. Stavrinidou and J. Rivnay, *Nature Materials*, 2020, **19**, 13-26.
19. V. Panchuk, I. Yaroshenko, A. Legin, V. Semenov and D. Kirsanov, *Anal Chim Acta*, 2018, **1040**, 19-32.
20. C. Vanhoof, J. R. Bacon, U. E. A. Fittschen and L. Vincze, *Journal of Analytical Atomic Spectrometry*, 2020, **35**, 1704-1719.
21. P. J. Potts, A. T. Ellis, M. Holmes, P. Kregsamer, C. Streli, M. West and P. Wobrauschek, *Journal of Analytical Atomic Spectrometry*, 2000, **15**, 1417-1442.
22. K. Nakayama and T. Nakamura, *X-Ray Spectrometry*, 2008, **37**, 204-209.
23. K. Sanyal, S. Chappa, J. Bahadur, A. K. Pandey and N. L. Mishra, *Journal of Analytical Atomic Spectrometry*, 2020, **35**, 2770-2778.
24. M. P. Nikiforov, B. Lai, W. Chen, S. Chen, R. D. Schaller, J. Strzalka, J. Maser and S. B. Darling, *Energy & Environmental Science*, 2013, **6**, 1513.

25. A. L. Oechsle, J. E. Heger, N. Li, S. Yin, S. Bernstorff and P. Müller-Buschbaum, *ACS Applied Materials & Interfaces*, 2022, **14**, 30802-30811.
26. J. Rivnay, S. Inal, B. A. Collins, M. Sessolo, E. Stavrinidou, X. Strakosas, C. Tassone, D. M. Delongchamp and G. G. Malliaras, *Nature Communications*, 2016, **7**.
27. C. M. Palumbiny, F. Liu, T. P. Russell, A. Hexemer, C. Wang and P. Müller-Buschbaum, *Adv Mater*, 2015, **27**, 3391-3397.
28. X. Jiang, P. Chotard, K. Luo, F. Eckmann, S. Tu, M. A. Reus, S. Yin, J. Reitenbach, C. L. Weindl, M. Schwartzkopf, S. V. Roth and P. Müller-Buschbaum, *Advanced Energy Materials*, 2022, **12**, 2103977.
29. G. E. Mohl, E. Metwalli and P. Muller-Buschbaum, *Acs Energy Lett*, 2018, **3**, 1525-1530.
30. M. D. Galluzzo, L. S. Grundy, C. J. Takacs, C. T. Cao, H. G. Steinriick, S. Fu, M. A. R. Valadez, M. F. Toney and N. P. Balsara, *Macromolecules*, 2021, **54**, 7808-7821.
31. R. H. Wu, B. D. Paulsen, Q. Ma and J. Rivnay, *Chem Mater*, 2022.
32. B. Y. Ouyang, C. W. Chi, F. C. Chen, Q. F. Xi and Y. Yang, *Advanced Functional Materials*, 2005, **15**, 203-208.
33. T. Takano, H. Masunaga, A. Fujiwara, H. Okuzaki and T. Sasaki, *Macromolecules*, 2012, **45**, 3859-3865.
34. C. M. Palumbiny, C. Heller, C. J. Schaffer, V. Korstgens, G. Santoro, S. V. Roth and P. Muller-Buschbaum, *J Phys Chem C*, 2014, **118**, 13598-13606.
35. E. Stavrinidou, P. Leleux, H. Rajaona, D. Khodagholy, J. Rivnay, M. Lindau, S. Sanaur and G. G. Malliaras, *Adv Mater*, 2013, **25**, 4488-4493.
36. O. Berezhetska, B. Liberelle, G. De Crescenzo and F. Cicoira, *J Mater Chem B*, 2015, **3**, 5087-5094.
37. Y. Y. Lee, G. M. Choi, S. M. Lim, J. Y. Cho, I. S. Choi, K. T. Nam and Y. C. Joo, *Sci Rep-Uk*, 2016, **6**.
38. M. A. Khan, S. P. Armes, C. Perruchot, H. Ouamara, M. M. Chehimi, S. J. Greaves and J. F. Watts, *Langmuir*, 2000, **16**, 4171-4179.
39. S. G. Im, K. K. Gleason and E. A. Olivetti, *Applied Physics Letters*, 2007, **90**, 152112.
40. A. E. Taouil, F. Lallemand, J. Y. Hihn, J. M. Melot, V. Blondeau-Patissier and B. Lakard, *Ultrason Sonochem*, 2011, **18**, 140-148.
41. D. Kim and I. Zozoulenko, *The Journal of Physical Chemistry B*, 2019, **123**, 5160-5167.

42. B. D. Paulsen, R. H. Wu, C. J. Takacs, H. G. Steinruck, J. Strzalka, Q. T. Zhang, M. F. Toney and J. Rivnay, *Adv Mater*, 2020, **32**.
43. A. V. Volkov, K. Wijeratne, E. Mitraka, U. Ail, D. Zhao, K. Tybrandt, J. W. Andreasen, M. Berggren, X. Crispin and I. V. Zozoulenko, *Advanced Functional Materials*, 2017, **27**.
44. H. Ling, L. Liu, P. S. Lee, D. Mandler and X. H. Lu, *Electrochim Acta*, 2015, **174**, 57-65.
45. S. Carli, M. Di Lauro, M. Bianchi, M. Murgia, A. De Salvo, M. Prato, L. Fadiga and F. Biscarini, *Acs Appl Mater Inter*, 2020, **12**, 29807-29817.
46. E. Stavrinidou, M. Sessolo, B. Winther-Jensen, S. Sanaur and G. G. Malliaras, *Aip Adv*, 2014, **4**.
47. E. Stavrinidou, P. Leleux, H. Rajaona, M. Fiocchi, S. Sanaur and G. G. Malliaras, *J Appl Phys*, 2013, **113**.
48. A. Giovannitti, R. B. Rashid, Q. Thiburce, B. D. Paulsen, C. Cendra, K. Thorley, D. Moia, J. T. Mefford, D. Hanifi, W. Y. Du, M. Moser, A. Salleo, J. Nelson, I. McCulloch and J. Rivnay, *Adv Mater*, 2020, **32**.
49. E. A. Schafer, R. H. Wu, D. Meli, J. Tropp, M. Moser, I. McCulloch, B. D. Paulsen and J. Rivnay, *Acs Appl Electron Ma*, 2022, **4**, 1391-1404.
50. E. Mitraka, M. Gryszel, M. Vagin, M. J. Jafari, A. Singh, M. Warczak, M. Mitrakas, M. Berggren, T. Ederth, I. Zozoulenko, X. Crispin and E. D. Glowacki, *Adv Sustain Syst*, 2019, **3**.
51. A. Kulkarni, S. Siahrostami, A. Patel and J. K. Norskov, *Chemical Reviews*, 2018, **118**, 2302-2312.
52. S. K. Singh, X. Crispin and I. V. Zozoulenko, *J Phys Chem C*, 2017, **121**, 12270-12277.
53. P. A. Gokturk, M. Barry, R. Segalman and E. J. Crumlin, *ACS Applied Polymer Materials*, 2020, **2**, 4752-4761.
54. J. L. Fulton, D. M. Pfund, S. L. Wallen, M. Newville, E. A. Stern and Y. J. Ma, *J Chem Phys*, 1996, **105**, 2161-2166.
55. M. Galib, M. D. Baer, L. B. Skinner, C. J. Mundy, T. Huthwelker, G. K. Schenter, C. J. Benmore, N. Govind and J. L. Fulton, *The Journal of Chemical Physics*, 2017, **146**, 084504.

56. A. Giovannitti, D. T. Sbircea, S. Inal, C. B. Nielsen, E. Bandiello, D. A. Hanifi, M. Sessolo, G. G. Malliaras, I. McCulloch and J. Rivnay, *P Natl Acad Sci USA*, 2016, **113**, 12017-12022.
57. A. Giovannitti, I. P. Maria, D. Hanifi, M. J. Donahue, D. Bryant, K. J. Barth, B. E. Makdah, A. Savva, D. Moia, M. Zetek, P. R. F. Barnes, O. G. Reid, S. Inal, G. Rumbles, G. G. Malliaras, J. Nelson, J. Rivnay and I. McCulloch, *Chemistry of Materials*, 2018, **30**, 2945-2953.
58. H. Bronstein, C. B. Nielsen, B. C. Schroeder and I. McCulloch, *Nature Reviews Chemistry*, 2020, **4**, 66-77.
59. V. Venkatraman, J. T. Friedlein, A. Giovannitti, I. P. Maria, I. McCulloch, R. R. McLeod and J. Rivnay, *Advanced Science*, 2018, **5**, 1800453.
60. S. T. M. Tan, A. Giovannitti, A. Marks, M. Moser, T. J. Quill, I. McCulloch, A. Salleo and G. E. Bonacchini, *Adv Mater*, 2022.
61. Z. Q. Liang, A. Nardes, D. Wang, J. J. Berry and B. A. Gregg, *Chemistry of Materials*, 2009, **21**, 4914-4919.
62. M. C. Jiang, J. F. Yuan, G. Z. Cao and J. J. Tian, *Chem Eng J*, 2020, **402**.
63. M. H. Li, J. Y. Shao, Y. Jiang, F. Z. Qiu, S. Wang, J. Zhang, G. Han, J. Tang, F. Wang, Z. Wei, Y. Yi, Y. W. Zhong and J. S. Hu, *Angewandte Chemie*, 2021, **133**, 16524-16529.
64. N. Li, A. B. Feng, X. B. Guo, J. M. Wu, S. D. Xie, Q. L. Lin, X. M. Jiang, Y. Liu, Z. L. Chen and X. T. Tao, *Adv Energy Mater*, 2022, **12**.
65. H. X. Xie, J. Liu, X. T. Yin, Y. X. Guo, D. Liu, G. F. Wang and W. X. Que, *Colloid Surface A*, 2022, **635**.
66. T. Muntasir and S. Chaudhary, *J Appl Phys*, 2015, **118**.
67. M. Arvind, C. E. Tait, M. Guerrini, J. Krumland, A. M. Valencia, C. Cocchi, A. E. Mansour, N. Koch, S. Barlow, S. R. Marder, J. Behrends and D. Neher, *J Phys Chem B*, 2020, **124**, 7694-7708.
68. G. Suppes, E. Ballard and S. Holdcroft, *Polym Chem-Uk*, 2013, **4**, 5345-5350.
69. S. Kwon, K. Yu, K. Kweon, G. Kim, J. Kim, H. Kim, Y. R. Jo, B. J. Kim, J. Kim, S. H. Lee and K. Lee, *Nature Communications*, 2014, **5**.
70. N. M. Nurazzi, N. Abdullah, S. Z. N. Demon, N. A. Halim and I. S. Mohamad, *Polymers-Basel*, 2021, **13**.

71. Y. Kim, H. Noh, B. D. Paulsen, J. Kim, I. Y. Jo, H. Ahn, J. Rivnay and M. H. Yoon, *Adv Mater*, 2021, **33**, 2007550.
72. S.-M. Kim, C.-H. Kim, Y. Kim, N. Kim, W.-J. Lee, E.-H. Lee, D. Kim, S. Park, K. Lee, J. Rivnay and M.-H. Yoon, *Nature Communications*, 2018, **9**.
73. N. Kim, S. Kee, S. H. Lee, B. H. Lee, Y. H. Kahng, Y.-R. Jo, B.-J. Kim and K. Lee, *Adv Mater*, 2014, **26**, 2268-2272.
74. E. J. Bae, Y. H. Kang, K. S. Jang and S. Y. Cho, *Sci Rep-Uk*, 2016, **6**.
75. R. Wu, B. D. Paulsen, Q. Ma and J. Rivnay, *Chemistry of Materials*, 2022.
76. B. A. Collins, J. E. Cochran, H. Yan, E. Gann, C. Hub, R. Fink, C. Wang, T. Schuettfort, C. R. McNeill, M. L. Chabinyc and H. Ade, *Nat Mater*, 2012, **11**, 536-543.
77. G. M. Newbloom, F. S. Kim, S. A. Jenekhe and D. C. Pozzo, *Macromolecules*, 2011, **44**, 3801-3809.
78. C.-Y. Chen, S.-H. Chan, J.-Y. Li, K.-H. Wu, H.-L. Chen, J.-H. Chen, W.-Y. Huang and S.-A. Chen, *Macromolecules*, 2010, **43**, 7305-7311.
79. E. M. Thomas, M. A. Brady, H. Nakayama, B. C. Popere, R. A. Segalman and M. L. Chabinyc, *Advanced Functional Materials*, 2018, **28**, 1803687.
80. B. D. Paulsen, A. Giovannitti, R. H. Wu, J. Strzalka, Q. T. Zhang, J. Rivnay and C. J. Takacs, *Small*, 2021, **17**.
81. S. Proller, F. Liu, C. H. Zhu, C. Wang, T. P. Russell, A. Hexemer, P. Muller-Buschbaum and E. M. Herzig, *Adv Energy Mater*, 2016, **6**.
82. L. Biessmann, L. P. Kreuzer, T. Widmann, N. Hohn, J. F. Moulin and P. Muller-Buschbaum, *Acs Appl Mater Inter*, 2018, **10**, 9865-9872.
83. C. J. Schaffer, C. M. Palumbiny, M. A. Niedermeier, C. Burger, G. Santoro, S. V. Roth and P. Muller-Buschbaum, *Adv Energy Mater*, 2016, **6**.